



HAL
open science

Electrical response of Pt/Ru/PbZr_{0.52}Ti_{0.48}O₃/Pt capacitor as function of lead precursor excess

Ibrahima Gueye, Gwenael Le Rhun, Olivier Renault, Emmanuel Defay,
Nicholas Barrett

► To cite this version:

Ibrahima Gueye, Gwenael Le Rhun, Olivier Renault, Emmanuel Defay, Nicholas Barrett. Electrical response of Pt/Ru/PbZr_{0.52}Ti_{0.48}O₃/Pt capacitor as function of lead precursor excess. Applied Physics Letters, 2017, 111 (22), pp.222902 - 222902. 10.1063/1.5004178 . hal-01664282

HAL Id: hal-01664282

<https://hal.science/hal-01664282v1>

Submitted on 14 Dec 2017

HAL is a multi-disciplinary open access archive for the deposit and dissemination of scientific research documents, whether they are published or not. The documents may come from teaching and research institutions in France or abroad, or from public or private research centers.

L'archive ouverte pluridisciplinaire **HAL**, est destinée au dépôt et à la diffusion de documents scientifiques de niveau recherche, publiés ou non, émanant des établissements d'enseignement et de recherche français ou étrangers, des laboratoires publics ou privés.

Electrical response of Pt/Ru/PbZr_{0.52}Ti_{0.48}O₃/Pt capacitor as function of lead precursor excess

Ibrahim Gueye,^{1,2} Gwenaél Le Rhun,^{1,2} Olivier Renault,^{1,2} Emmanuel Defay,³ and Nicholas Barrett^{4,a)}

¹Univ. Grenoble Alpes, F-38000 Grenoble, France

²CEA, LETI, MINATEC Campus, F-38054 Grenoble, France

³Material Research and Technology Department, Luxembourg Institute of Science and Technology, 41 Rue du Brill, L-4422 Belvaux, Luxembourg

⁴SPEC, CEA, CNRS, Université Paris Saclay, F-91191 Gif-sur-Yvette, France

(Received 11 September 2017; accepted 11 November 2017; published online 30 November 2017)

We investigated the influence of the surface microstructure and chemistry of sol-gel grown PbZr_{0.52}Ti_{0.48}O₃ (PZT) on the electrical performance of PZT-based metal-insulator-metal (MIM) capacitors as a function of Pb precursor excess. Using surface-sensitive, quantitative X-ray photoelectron spectroscopy and scanning electron microscopy, we confirm the presence of ZrO_x surface phase. Low Pb excess gives rise to a discontinuous layer of ZrO_x on a (100) textured PZT film with a wide band gap reducing the capacitance of PZT-based MIMs whereas the breakdown field is enhanced. At high Pb excess, the nanostructures disappear while the PZT grain size increases and the film texture becomes (111). Concomitantly, the capacitance density is enhanced by 8.7%, and both the loss tangent and breakdown field are reduced by 20 and 25%, respectively. The role of the low permittivity, dielectric interface layer on capacitance and breakdown is discussed.

Published by AIP Publishing. <https://doi.org/10.1063/1.5004178>

Ferroelectric Pb(Zr,Ti)O₃ (PZT) thin films are envisaged in the new generation of decoupling multiple metal-insulator-metal (MIM) stacks showing enhanced capacitance density and breakdown voltage.¹ The gain in capacitance is achieved, thanks to the multi-MIM structure, however, device performance is determined not only by the bulk dielectric properties but also by the interface with the electrodes.^{2,3} In this context, it is important to engineer interface chemistry which does not degrade the multi-MIM capacitive performance.

Sol-gel synthesis is well adapted for mass production of PZT, but because of Pb loss during the necessary crystallization annealing,^{4,5} excess Pb in the precursor solution is required to obtain near-stoichiometric PZT films.^{6,7} In turn, excess Pb may change the surface composition, modifying the PZT/electrode interface chemistry and hence the electrical response of the capacitor. For example, it has been shown that the surface phase of PZT with 10% of Pb precursor excess is not pyrochlore or fluorite as previously thought, but ZrO_{1.82–1.89}.⁸ This creates a low permittivity, dielectric layer at the interface which may play an important role in the capacitor performance.

We present a systematic study of the sol-gel surface chemistry and structure and the electrical characteristics of PZT-based capacitor, in particular, the breakdown field (E_{BD}) and the capacitance density, as a function of Pb excess in the precursor solution. The surface microstructure was imaged by scanning electron microscopy (SEM), the crystallographic orientation measured by X-ray diffraction (XRD), while the surface chemistry and stoichiometry studied by quantitative X-ray photoelectron spectroscopy (XPS). The chemical and structural characterization is correlated with standard C-V, loss tangent, and breakdown voltage measurements of the PZT-based MIM capacitors.

The samples were prepared at the MINATEC High-Technologies Building cleanrooms of CEA-LETI (Grenoble). The details of the sol-gel layer growth are given elsewhere.⁸ The 220 nm PZT films close to the morphotropic phase boundary (PbZr_{0.52}Ti_{0.48}O₃) are made of four successive 55 nm sol-gel layers. Four Pt(100 nm)/Ru(5 nm)/PZT(220 nm)/Pt/TiO₂/SiO₂/Si samples were prepared, each consisting of two 55 nm sol-gel films with 10% excess Pb sandwiched between the seed and the top sol-gel layer. The Pb excess of both the seed and the top layer was set to 10, 15, 20, and 30% for the four samples. Brewer *et al.* have recently demonstrated that the Ti/Zr concentration gradient can be reduced by increasing the number of sol-gel layers (i.e., by decreasing the individual sol-gel layer thickness) and hence the number of annealing steps.⁹ Here, we have focused rather on the influence of the Pb excess. The Pt(100 nm)/Ru(5 nm) top electrode was deposited using DC magnetron sputtering. Pt/Ru leads to better saturation capacitance and breakdown voltage than Pt, and the Ru interlayer ensures better adhesion of the Pt, avoiding delamination in the case of multi-MIM structure (manuscript in preparation). The full layers were lithographically etched to give a set of 80 × 80 μm² capacitors.

A HP4284A Agilent capacitance meter was used for the capacitance (C) and dielectric loss measurement. C(V) and loss tangent [tanδ(V)] characteristics were acquired at room temperature between −10 V and +10 V with a 10 kHz, sinusoidal excitation signal and an amplitude of 100 mV. E_{BD} was measured using Linear Ramp Voltage Stress test ($\Delta V = 0.5$ V and $\Delta t = 0.5$ s) and Weibull statistical analysis. With an appropriate trigger on the current, the voltage at which the capacitor has shorted can be detected and recorded. As the E_{BD} follows a probability law, by cumulating breakdown voltage data over 90 capacitors tested per wafer, the repartition function can be fitted and breakdown voltage can be extracted.

^{a)}Author to whom correspondence should be addressed: nick.barrett@cea.fr

For all electrical measurements, the bias is applied to the bottom electrode and top electrode is grounded. SEM was carried out in the secondary electron (SE) detection mode with a Hitachi-4160 scanning electron microscope (30 kV primary electron beam, 15 mA emission current, and chamber pressure 7 mbar).⁸

XRD (θ - 2θ) was performed using a XPERT-PRO MRD XL from PANalytical, using Cu K α radiation ($\lambda = 0.15418$ nm).¹⁰

XPS analysis of the sol-gel layers was carried out at a base pressure of 5×10^{-10} mbar in a Multiprobe system (ScientaOmicron) with a monochromatic Al K α X-ray source (1486.6 eV) and a 128-channel Argus electron analyzer.¹¹ The take-off angle, defined as the angle between the analyzer axis and the sample surface, was 70° .¹² Samples were mounted with double-side conductive tape onto the metallic sample holder. The overall energy resolution (X-ray source bandwidth and spectrometer resolution) was 0.27 eV for the core-level spectra. The binding energy was calibrated using the C 1s emission. CasaXPS software was used for data analysis.¹³ After Shirley background subtraction, the core level spectra were fitted using Gaussian-Lorentzian line-shapes. The line-shape and width were fixed for each core level.⁸

The C-V curves are presented in Fig. 1(a). They show the characteristic butterfly loop of a ferroelectric. The curves are not symmetric about zero field but are shifted. The shift is 34.0 kV/cm for PZT30 and 39.8 kV/cm for PZT10, 15 and 20, indicating a downwards pointing imprint polarization for all as grown films. The curves are offset for clarity by 15 nF/mm² per curve. The coercive field with respect to the symmetry point is ± 17.4 kV/cm. Figure 1(b) shows the maximum capacitance density and loss tangent as a function of

Pb excess. The maximum capacitance density increases from 46.2 to 50 nF/mm² between 10 and 20% Pb excess. At 30% Pb excess, the capacitance density is 48.9 nF/mm². On the other hand, passing from 10 to 30% Pb, the loss tangent decreases from 0.0453 to 0.0367.

Figure 1(c) show the evolution of current as function of electric field during the E_{BD} measurement. Low field, peak current densities of 1.4×10^{-5} (92.6 kV/cm), 1.8×10^{-6} (115.7 kV/cm), 1.8×10^{-6} (115.7 kV/cm), and 2.0×10^{-6} A/cm² (115.7 kV/cm) are recorded for PZT10, PZT15, PZT20, and PZT30, respectively. Above 200 kV/cm, a nearly constant current density is observed for all excess Pb values. Beyond 750 kV/cm, the sharp increase in the current leads rapidly to breakdown as illustrated in Fig. 1(c). E_{BD} was defined for an abrupt current increase, typically greater than a decade, in a single voltage step (0.5 V in our case) leading to short-circuit of the capacitor. Figure 1(d) shows E_{BD} , obtained by a Weibull statistical analysis, as a function of Pb precursor excess. The error bar is given by the size of the square symbols. E_{BD} decreases from 1.60 to 1.26 MV/cm as the Pb excess increases from 10 to 30% with a maximum of 1.68 MV/cm at 15% excess Pb. Thus, capacitance density increases by 8.7% with Pb excess whereas both the loss tangent and E_{BD} decrease, respectively, by 20 and 25%.

Figure 2 shows the surface microstructure of PZT 10, 15, 20, and 30. Above 20% Pb excess [Fig. 2(c)], the surface phase is absent whereas for 10% Pb excess it covers 1/5th of the PZT surface. In addition, the PZT grain size increases with Pb excess and the number of grain boundaries decreases. The structural analysis is completed by the X-ray diffraction θ - 2θ scans in Fig. 3 which show the effect of Pb precursor excess on the preferred film orientation. The film

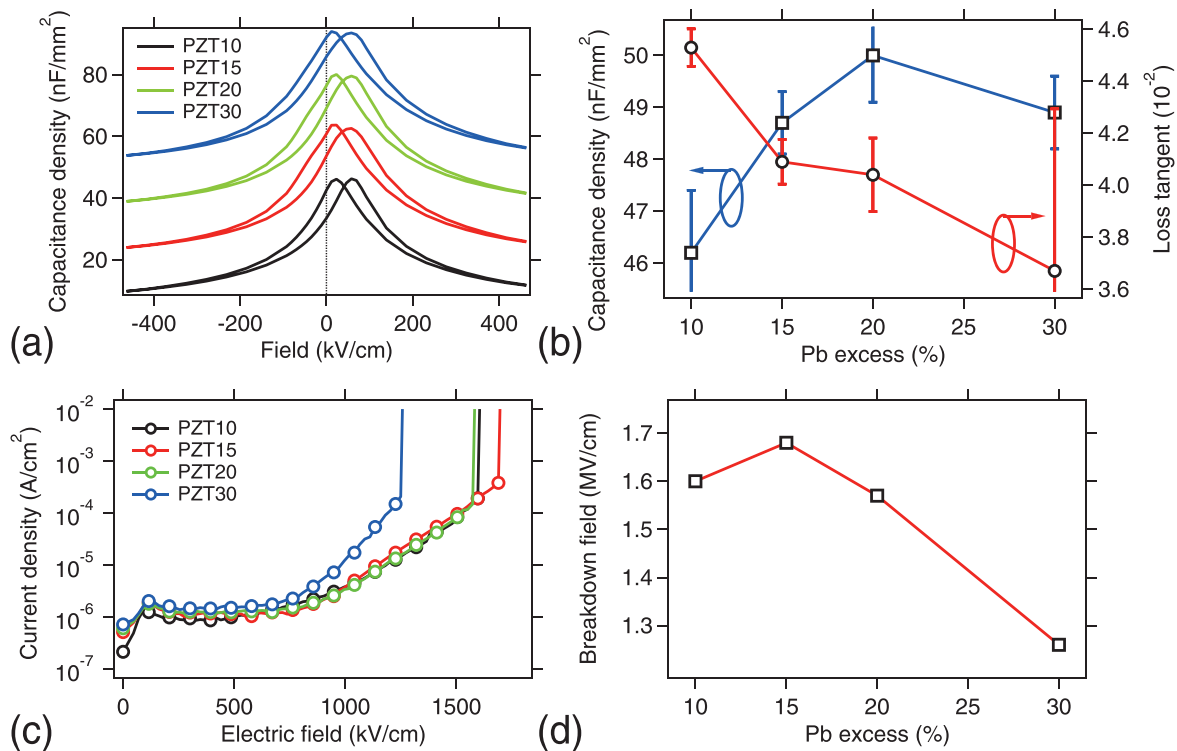


FIG. 1. PZT 10, 15, 20, and 30 (a) capacitance as a function of applied field. (b) Maxima of surface capacitance density and loss tangent as a function of Pb excess. (c) Typical I-V curve recorded during E_{BD} measurement (d) E_{BD} as function of Pb excess.

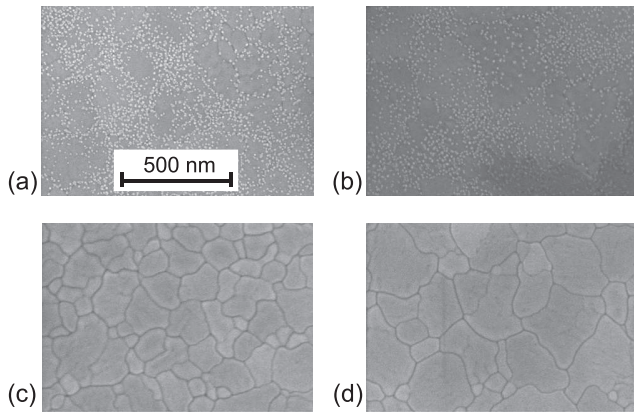


FIG. 2. SEM images of as deposited (a) PZT10, (b) PZT15, (c) PZT20, and (d) PZT30. The scale bar is the same for all images.

texture changes from (100) to (111) as the Pb excess increases from 10 to 30%. The ZrO_x surface phase is not visible in the XRD scans because the signal is too weak. Indeed, one needs to use glancing angle XRD in order to detect the crystallinity of the ZrO_x nanostructures.⁸

The XPS spectra, normalized with respect to the continuous background at high kinetic energy, are presented in Fig. 4. Figures 4(a) and 4(b) present the Pb 4f and Ti 2p_{3/2} core levels. The binding energy of the Pb 4f peak does not shift with Pb excess but the intensity increases for 30% with respect to 10% Pb. This implies that, whilst there is no change in the Pb chemical environment or valence state, the concentration does increase with excess Pb. We estimate the Pb surface concentration to be 19.6, 24, 25.8, to 24.1% for PZT 10, 15, 20, and 30%, respectively. The error bar of the relative atomic concentration is $\pm 5\%$, the variations in the Pb concentration are therefore significant apart from between PZT15 and PZT30. The Pb surface concentration varies little for higher Pb precursor excess due to the effect of vapor pressure on volatility during the sol-gel process. The Ti 2p_{3/2} spectrum in Fig. 4(b) reveals a low level of Ti at the surface with concentration of only 3.4, 2.8, 2.7, and 3.2% for PZT 10, 15, 20, and 30, respectively. This is expected since the Ti crystallizes at the beginning of the sol-gel process giving a strong Ti concentration gradient.^{14,15} Like the Pb 4f, the Ti 2p binding energy does not change and the Ti environment is unaffected by the presence of the secondary phase present at the surface.

The Zr 3d and O 1s spectra are presented in Figs. 4(c) and 4(d). The components Zr_I and O_I characterize the PZT

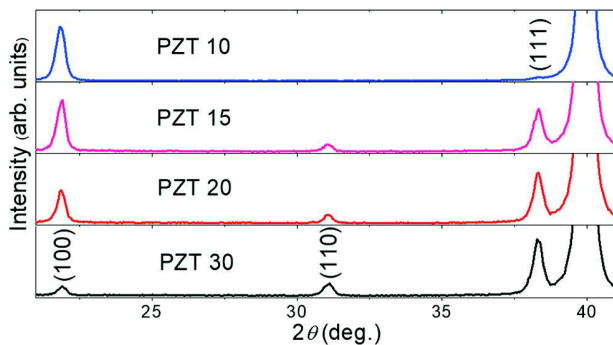


FIG. 3. θ - 2θ XRD scans for 10, 15, 20, and 30% Pb precursor excess.

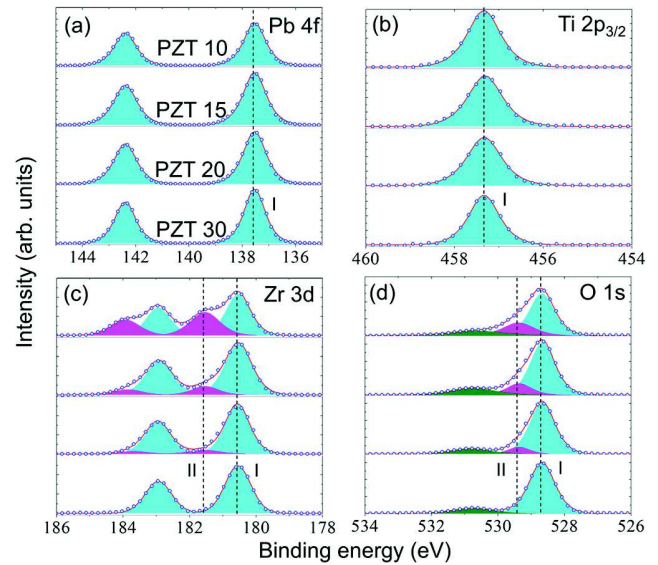


FIG. 4. (a) Pb 4f, (b) Ti 2p_{3/2}, (c) Zr 3d, and (d) O 1s core level spectra for PZT10, 15, 20, and 30. Open circles are the experimental points red lines the best fit, colored peaks the different components. In each panel, the uppermost (lowermost) spectrum is that of PZT10 (PZT30). The main peak I (light gray, turquoise online) corresponds to the perovskite structure; gray peak II (magenta online) surface phase and low intensity, green peaks (O_{III}) to surface contamination.

while the components Zr_{II} and O_{II} are due to the ZrO_x surface phase.⁸ In Figs. 4(c) and 4(d), the Zr_{II} and O_{II} components decrease with increasing Pb excess, confirming that low Pb content favors the formation of ZrO_x nanostructures. Components Zr_I and O_I, characteristic of the PZT film, are anti-correlated with the Zr_{II} and O_{II} intensities since their intensities are attenuated by the overlying ZrO_x nanostructures. Thus, the higher the nanostructure density, the lower the intensity measured from the underlying PZT. The O_{III} component is related to surface contamination. The estimated atomic concentrations are given in Table I.

The volatility of PbO during recrystallization leads to sub-stoichiometric Pb content and therefore interruption of the PZT grain coalescence,¹⁶ indeed Fig. 2 shows that the PZT grain size decreases between 30% and 10% Pb excess. The sol-gel layer has a concentration gradient of Zr and Ti¹⁴ with the highest concentration of Ti near the bottom and the Zr at the surface of each PZT layer. The Zr/Ti gradient results from the crystallization temperatures.^{15,17} Almost all of Ti is transformed into the perovskite phase whereas the excess ZrO_2 is found at the surface in the form of secondary

TABLE I. PZT surface composition based on the XPS intensities and relative sensitivity factors. The uncertainty in relative atomic concentration is estimated to be less than $\pm 5\%$.

	PZT10	PZT15	PZT20	PZT30
Pb	19.6	24.0	25.8	24.1
Ti	3.4	2.8	2.7	3.2
Zr _I	9.4	11.4	13.1	14.2
Zr _{II}	7.1	5.2	2.6	...
O _I	35.9	38.7	43.1	50.3
O _{II}	14.1	8.5	4.2	...
O _{III}	10.5	9.4	8.5	8.2

phase. Lack of PbO creates the rupture of the chemical reaction at the origin of the formation of PZT, favoring the formation of ZrO_x at the film surface. Using the relative XPS Zr_{II} and O_{II} intensities in Table I and with the sensitivity factors of each elements, we estimate the stoichiometry of the surface phase to be $ZrO_{1.98}$, $ZrO_{1.63}$ and $ZrO_{1.61}$ for the PZT10, 15 and 20, respectively. Given the XPS uncertainty of 5% in the relative atomic concentration the variation in the nanostructure stoichiometry is also significant. We should point out that as the XPS probing depth is much less than the average nanostructure size, this may only reflect the surface composition of the nanostructure. Furthermore, the change in the absolute XPS intensities confirms the ZrO_x surface phase enrichment for low Pb excess.

As shown by the XRD analysis, Pb excess also impacts the crystallographic orientation of the films.^{18,19} An increase in the PZT grain size of the favors the (111) orientation as observed on PZT 20 and PZT30, whereas for PZT10 with small grain size the crystallographic orientation is predominantly (100).

The lower permittivity of ZrO_x should reduce the capacitance density of the PZT-based MIM device. We can estimate the effect of the surface phase on the overall capacitance density using a simple, two-layer model which considers the ZrO_x as a dielectric layer in series with the PZT. Letting θ be the fractional coverage of the ZrO_x nanostructures, the total capacitance can be written $C_{total} = C_\theta + C_{1-\theta}$, where $C_\theta = \theta \times C_{ZrO_x} C_{PZT} / (C_{ZrO_x} + C_{PZT})$ and $C_{1-\theta} = C_{PZT} (1 - \theta)$. From the microstructure shown in Fig. 2 and the XPS Zr_{II} intensities reported in Table I, $\theta = 0.195, 0.15, 0.05$, and 0 for PZT10, 15, 20, and 30, respectively. Assuming a relative permittivity of 900 and 25 for PZT and ZrO_x , and using the standard formula for the capacitance $C = \epsilon_0 \epsilon A/t$, gives $C_{PZT10} \sim 0.86.C_{PZT30}$, $C_{PZT15} \sim 0.89.C_{PZT30}$, and $C_{PZT20} \sim 0.96.C_{PZT30}$, in good agreement with the experimental capacitance densities. The variation in capacitance density is therefore mainly a result of the low dielectric constant ZrO_x interface phase. However, the absolute values of capacitance density are slightly overestimated (46, 48, 51, and 53 nF/mm²). This could be due to a thin dead layer between the clean PZT surface and the Pt/Ru electrode. The change of crystallographic orientation with Pb excess rate might also contribute to the capacitance density.²⁰ The slight dip in the capacitance density for 30% Pb excess may be due to the strong reduction of (100) oriented PZT together with the emergence of mainly (111)-oriented film as reported in Table II. A second possible reason is the start of the formation of a PbO phase for high Pb precursor excess. The much lower permittivity of PbO could also be responsible for the reduction in capacitance density. Confirmation of this would require a very high resolution

TABLE II. Percentage fraction of PZT crystallographic orientation as a function of Pb excess.

	PZT10	PZT15	PZT20	PZT30
(100)	92.4	41.2	27.7	9.4
(110)	0.4	1.9	2.2	3.3
(111)	7.2	56.9	70.1	87.3

XPS study in order to distinguish the PZT and PbO core level components.

The higher loss tangent [Fig. 1(a)] at low Pb excess may be due to the extra grain boundaries favoring the creation of defects and therefore more loss mechanisms. With increasing the Pb excess content and grain size, the loss tangent decreases.

Finally, E_{BD} also decreases, by 25%, with increasing Pb excess. PbO has a smaller band gap [1.9 eV (Ref. 21)] than PZT but the same valence state. One hypothesis is that the residual PbO, present at a concentration below the XPS sensitivity increases the number of mobile charge carriers¹⁸ and creates conducting paths following a percolation model,^{22,23} leading to earlier breakdown. On the other hand, the Zr oxide layer at the interface with the electrode may increase E_{BD} since the 5.8 eV band gap of ZrO_2 (Ref. 24) is significantly greater than that of PZT. The electrical performance of a PZT-based MIM capacitor is therefore a sensitive function of the Pb excess used in the precursor solution during synthesis. Low Pb content induces a wide band gap ZrO_x surface layer which increases by 25% E_{BD} but reduces the total capacitance. The role of the sol-gel internal interfaces should also be studied.

We have studied the correlations between electrical properties of PZT-based MIM capacitors and modifications of the surface microstructure and chemistry as a function of Pb precursor excess. Low levels of Pb precursor excess leads to the formation of ZrO_x nanostructures at the surface of the sol-gel layer. Higher Pb content allows the PZT to proceed to its end-point fully consuming the ZrO_2 precursor. As a result, the density of surface nanostructures decreases, vanishing completely above 20% Pb excess. In addition, the crystallographic orientation evolves from (100) to (111) when passing from 10 to 30% Pb excess. From the point of view of the electrical characteristics of the PZT-based MIM, excess Pb precursor has opposite effects on the capacitance density and E_{BD} . The presence of ZrO_x based nanostructures at the sol-gel film surface using low Pb excess reduces the capacitance density by 8.7%, whereas high Pb reduces E_{BD} by 25%. The relative importance of residual PbO and the ZrO_x surface phase for E_{BD} remains to be determined.

I.G. was funded by a CEA CTBU research grant. We acknowledge the support from the Nanocharacterization Platform of CEA-MINATEC and from the CEA operando project. E.D. was funded by FNR through the COFERMAT project P12/4853155.

¹M. Klee, H. Boots, B. Kumar, C. V. Heesch, R. Mauczuk, W. Keur, M. D. Wild, H. V. Esch, A. L. Roest, K. Reimann, L. V. Leuken, O. Wunnicke, J. Zhao, G. Schmitz, M. Mienkina, M. Mleczko, and M. Tiggelman, *IOP Conf. Ser.: Mater. Sci. Eng.* **8**, 012008 (2010).

²L. Pintilie, I. Pasuk, R. Negrea, L. D. Filip, and I. Pintilie, *J. Appl. Phys.* **112**, 64116 (2012).

³M.-G. Han, M. S. Marshall, L. Wu, M. A. Schofield, T. Aoki, R. Twisten, J. Hoffman, F. J. Walker, C. H. Ahn, and Y. Zhu, *Nat. Commun.* **5**, 4693 (2014).

⁴K. Li, N. Sama, T. Li, D. Rémiens, G. Du, X. Dong, and G. Wang, *Appl. Phys. Lett.* **104**, 092904 (2014).

⁵R. L. Holman and R. M. Fulrath, *J. Appl. Phys.* **44**, 5227 (1973).

⁶A. Etin, G. E. Shter, R. Brener, S. Baltianski, and G. S. Grader, *J. Am. Ceram. Soc.* **90**, 3800 (2007).

⁷S. P. Bag, J.-L. Her, and T.-M. Pan, *Ceram. Int.* **42**, 18402 (2016).

- ⁸I. Gueye, G. Le Rhun, P. Gergaud, O. Renault, E. Defay, and N. Barrett, *Appl. Surf. Sci.* **363**, 21 (2016).
- ⁹S. J. Brewer, S. C. Williams, C. Z. Deng, A. B. Naden, S. M. Neumayer, B. J. Rodriguez, A. Kumar, and N. Bassiri-Gharb, *J. Am. Ceram. Soc.* **100**, 5561 (2017).
- ¹⁰J. Yu, L. Liu, S. Jin, H. Zhou, X. He, C. Zhang, W. Zhou, X. Wang, X. Chen, and C. Chen, *J. Solid State Chem.* **184**, 2790 (2011).
- ¹¹E. Martinez, A. Herrera-Gomez, M. Allain, O. Renault, A. Faure, A. Chabli, and F. Bertin, *J. Vac. Sci. Technol., A* **30**, 040605 (2012).
- ¹²V. Lockett, R. Sedev, C. Bassell, and J. Ralston, *Phys. Chem. Chem. Phys.* **10**, 1330 (2008).
- ¹³J. L. Wang, F. Gaillard, A. Pancotti, B. Gautier, G. Niu, B. Vilquin, V. Pillard, G. L. M. P. Rodrigues, and N. Barrett, *J. Phys. Chem. C* **116**, 21802 (2012).
- ¹⁴J. Abergel, M. Allain, H. Michaud, M. Cuffe, T. Ricart, C. Dieppedale, G. Le Rhun, D. Faralli, S. Fanget, and E. Defay, in *IEEE International Ultrasonics Symposium (IUS)* (2012), pp. 972–974.
- ¹⁵F. Calame and P. Muralt, *Appl. Phys. Lett.* **90**, 062907 (2007).
- ¹⁶A. Zomorrodian, A. Mesarwi, N. J. Wu, and A. Ignatiev, *Appl. Surf. Sci.* **90**, 343 (1995).
- ¹⁷A. P. Wilkinson, J. S. Speck, A. K. Cheetham, S. Natarajan, and J. M. Thomas, *Chem. Mater.* **6**, 750 (1994).
- ¹⁸M. I. Yanovskaya, I. E. Obvintseva, L. I. Solovyova, E. P. Kovsman, K. A. Vorotilov, and V. A. Vasilyev, *Integr. Ferroelectr.* **19**, 193 (1998).
- ¹⁹C. S. Park, J. W. Lee, S. M. Lee, S. H. Jun, and H. E. Kim, *J. Electroceram.* **25**, 20 (2010).
- ²⁰X.-H. Du, J. Zheng, U. Belegundu, and K. Uchino, *Appl. Phys. Lett.* **72**, 2421 (1998).
- ²¹G. Trinquier and R. Hoffmann, *J. Phys. Chem.* **88**, 6696 (1984).
- ²²R. Degraeve, G. Groeseneken, R. Bellens, J. L. Ogier, M. Depas, P. J. Roussel, and H. E. Maes, *IEEE Trans. Electron Devices* **45**, 904 (1998).
- ²³M. T. Chentir, J. B. Jullien, B. Valtchanov, E. Bouyssou, L. Ventura, and C. Anceau, *Microelectron. Reliab.* **49**, 1074 (2009).
- ²⁴P. W. Peacock and J. Robertson, *J. Appl. Phys.* **92**, 4712 (2002).